

Sulfur K-Edge X-ray Absorption Spectroscopy and Density Functional Theory Calculations on Monooxo Mo^{IV} and Bisoxo Mo^{VI} Bis-dithiolenes: Insights into the Mechanism of Oxo Transfer in Sulfite Oxidase and Its Relation to the Mechanism of DMSO Reductase

Yang Ha,[†] Adam L. Tenderholt,^{†,‡} Richard H. Holm,^{*,§} Britt Hedman,^{*,‡} Keith O. Hodgson,^{*,†,‡} and Edward I. Solomon^{*,†,‡}

[†]Department of Chemistry, Stanford University, Stanford, California 94305, United States

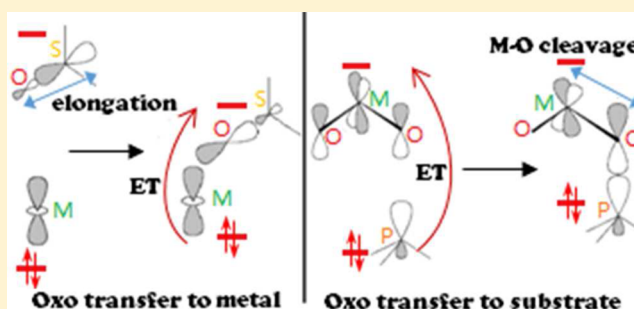
[‡]Stanford Synchrotron Radiation Lightsource, SLAC, Stanford University, Menlo Park, California 94025, United States

[§]Department of Chemistry and Chemical Biology, Harvard University, Cambridge, Massachusetts 02138, United States

S Supporting Information

ABSTRACT: Sulfur K-edge X-ray absorption spectroscopy (XAS) and density functional theory (DFT) calculations have been used to determine the electronic structures of two complexes [Mo^{IV}O(bdt)₂]²⁻ and [Mo^{VI}O₂(bdt)₂]²⁻ (bdt = benzene-1,2-dithiolate(2-)) that relate to the reduced and oxidized forms of sulfite oxidase (SO). These are compared with those of previously studied dimethyl sulfoxide reductase (DMSOr) models. DFT calculations supported by the data are extended to evaluate the reaction coordinate for oxo transfer to a phosphite ester substrate. Three possible transition states are found with the one at lowest energy, stabilized by a P–S interaction, in good agreement with experimental kinetics data.

Comparison of both oxo transfer reactions shows that in DMSOr, where the oxo is transferred from the substrate to the metal ion, the oxo transfer induces electron transfer, while in SO, where the oxo transfer is from the metal site to the substrate, the electron transfer initiates oxo transfer. This difference in reactivity is related to the difference in frontier molecular orbitals (FMO) of the metal–oxo and substrate–oxo bonds. Finally, these experimentally related calculations are extended to oxo transfer by sulfite oxidase. The presence of only one dithiolene at the enzyme active site selectively activates the equatorial oxo for transfer, and allows facile structural reorganization during turnover.



1. INTRODUCTION

Molybdenum is the one second row transition metal that has been found in almost all forms of life, including microorganisms, plants and animals.¹ It is part of a multinuclear active site in the FeMoco cofactor in nitrogenase,^{2,3} while most other enzymes have a mononuclear center, which is redox-active between the Mo^{IV} and Mo^{VI} oxidation states and has pyranopterin-dithiolene ligands.^{4–7} The Mo^V oxidation state is not directly involved in the oxo transfer reaction, but is involved as enzymes and models cycle between Mo^{IV} (d²) and Mo^{VI} (d⁰) oxidation states.⁸ These mononuclear molybdenum enzymes have been divided into three families: dimethyl sulfoxide (DMSO) reductases, sulfite oxidases, and xanthine oxidases.⁶ DMSO reductase and sulfite oxidase catalyze oxo-transfer reactions. DMSO reductase reduces DMSO to DMS (dimethyl sulfide), with oxo transfer to the Mo center, which converts from a Mo^{IV} desoxo (i.e., no oxo ligand, but a with an alkoxide–Mo bond) to a Mo^{VI} monooxo species. Sulfite oxidase (SO) transfers an oxo ligand to substrates, converting the Mo center from a Mo^{VI} bisoxo to a Mo^{IV} monooxo species.⁵

Model complexes have been synthesized and characterized that mimic either the structure and/or activity for these enzyme active sites. These have greatly assisted in developing an understanding of the mechanisms of oxo transfer to Mo^{IV} and oxo transfer from Mo^{VI}O₂.⁹ A number of experimental and theoretical studies have focused on DMSO reductase reactions to understand the geometric and electronic structural contributions to function.^{10–15} Our previous study of [Mo^{IV}(OSi)(bdt)₂][–] and [Mo^{VI}O(OSi)(bdt)₂][–] complexes (OSi = [OSiPh₂tBu][–], bdt = benzene-1,2-dithiolate(2-)), Figure 1B,D), provided the following insight into the nature of the DMSO oxo transfer reaction:¹⁰ (1) the dithiolene ligands are innocent (i.e., not redox-active), but are strong π -donors that stabilize the singlet ground state of the Mo^{IV} in the absence of a strong oxo ligand; and (2) in the oxo transfer from the DMSO to the Mo^{IV} center, the S–O bond elongation polarizes the bond, and decreases the energy gap between frontier molecular

Received: April 10, 2014

Published: June 2, 2014

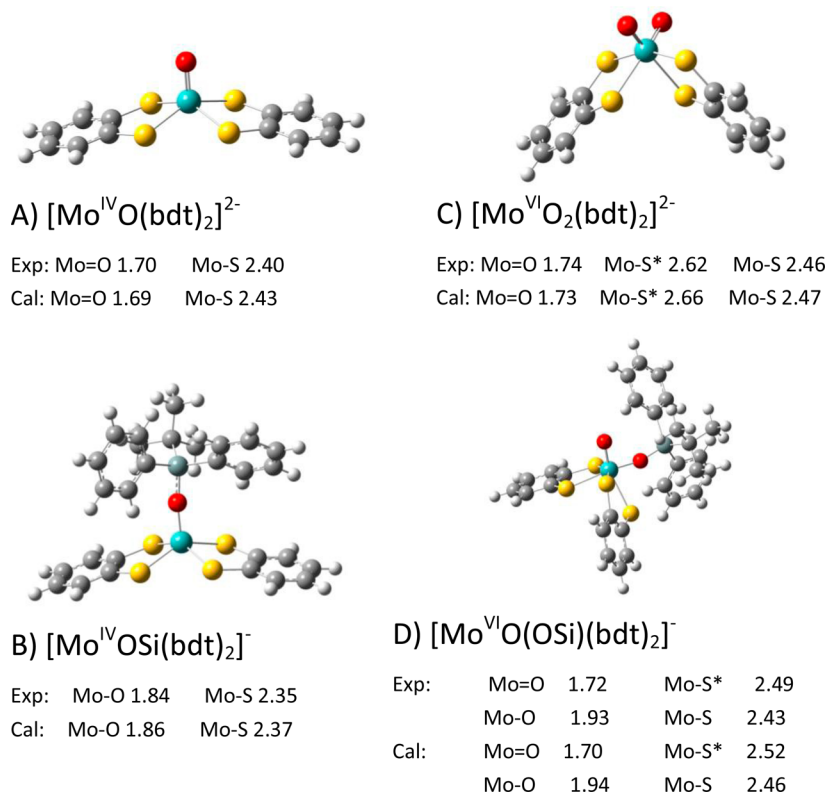
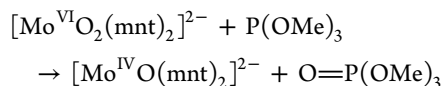


Figure 1. Crystal and geometry optimized structures of the complexes in this study. Bond distances in angstroms (Å) are listed below the structure. Mo–S* indicates the sulfur atom that is trans-axial to the oxo ligand. In panel D, similar Mo–S bond distances were averaged.

orbitals (FMOs, the LUMO on the substrate and the HOMO occupied d-orbital on the Mo^{IV}), allowing the transfer of the electron pair from Mo to the substrate to complete the oxo transfer.

There have also been a number of sulfite oxidase model studies. Holm and co-workers have synthesized a model that matched the native enzyme structure well, but there was no reported reactivity.¹⁶ The Sarkar group measured the kinetics of oxo transfer from $[\text{Mo}^{\text{VI}}\text{O}_2(\text{mnt})_2]^{2-}$ (mnt = maleonitriledithiolate(2-)) to HSO_3^- and found Michaelis–Menten kinetics.¹⁷ Other model studies focused on the transfer of an oxo group from a $\text{Mo}^{\text{VI}}\text{O}_2$ species to phosphine substrates. Hall and co-workers studied the reaction: $[\text{Mo}^{\text{VI}}\text{O}_2(\text{tBuL-NS})_2] + \text{PMe}_3 \rightarrow [\text{Mo}^{\text{IV}}\text{O}(\text{tBuL-NS})_2] + \text{OPMe}_3$ computationally¹⁸ based on the experimental data of Holm and co-workers on this reaction.¹⁹ The tBuL-NS ligand had nonconjugated nitrogen and sulfur groups bound to the Mo. Basu and co-workers²⁰ studied the reaction: $[\text{L}^{\text{IPr}}\text{MoO}_2(\text{OPh})] + \text{PMe}_3 \rightarrow [\text{L}^{\text{IPr}}\text{MoO}(\text{OPh})\text{-Solvent}] + \text{O}=\text{PMe}_3$ both experimentally and computationally, where L^{IPr} is a tridentate ligand with nitrogens bound to Mo.²⁰ Neither study utilized the dithiolene ligation present in the enzymes. There are also studies to evaluate electronic structures of model complexes that do not have oxo transfer reactivity, but contain dithiolene ligation.^{21,22} The Holm group has synthesized a series of $\text{Mo}^{\text{IV}}\text{O}$ and $\text{Mo}^{\text{VI}}\text{O}_2$ bis-dithiolene complexes, characterized their geometric structures and showed that they undergo oxo transfer to phosphite esters with well determined kinetics parameters for the reaction²³



The focus of the current study is to use spectroscopic and computational methods to determine the electronic structure of these Mo dithiolene complexes, and use experimentally calibrated calculations to evaluate this oxo transfer reaction. The goal is to understand this and the other oxo transfers to substrate on a molecular level and to compare these to the reaction coordinate obtained for DMSO reductase, which involves oxo transfer from substrate to Mo^{IV} .

In our previous study of the DMSO reductase reaction, S K-edge X-ray absorption spectroscopy (XAS) was used to experimentally determine the electronic structures of the dithiolene coordinated Mo centers.¹⁰ The transition of a S 1s electron into the low-lying unoccupied valence orbitals, which have some S 3p character mixed into predominantly metal d-orbitals, leads to pre-edge features in XAS. The energies of the pre-edge transitions reflect the energies of these unoccupied Mo d-orbitals, which depend on the effective nuclear charge (Z_{eff}) of the metal and the ligand field strength.²⁴ Thus, changing from Mo^{IV} to Mo^{VI} will shift the pre-edge to lower energy, while binding a strong (i.e., oxo) ligand will shift the $d\sigma$ and dx orbitals to higher energy. Of particular utility is that the intensity of a pre-edge transition is proportional to the amount of S 3p character mixed into the unoccupied metal d orbitals due to covalent bonding. Thus, the metal–sulfur bond covalencies can be measured experimentally.

The intensity of a pre-edge peak D_0 is given by

$$D_0 = \sum c\alpha^2 |\langle S_{1s} | r | S_{3p} \rangle|^2 = \frac{\alpha^2 h}{3N} I_s \quad (1)$$

where α^2 is the bond covalency (i.e., sulfur p character mixed into a metal d orbital), N is the total number of sulfurs bound to the metal, h is the total number of d electron holes, and I_s is

the electric dipole integral, which is dependent on the Z_{eff} of the S ligand and has been experimentally determined in reference.²⁵ Density functional theory (DFT) calculations supported by the S K-edge XAS data can then provide further insight into the bonding and be used to explore the reactivity.²⁶

In this study, S K-edge XAS is used to experimentally determine the electronic structures of the dithiolene complexes $[\text{Mo}^{\text{IV}}\text{O}(\text{bdt})_2]^{2-}$ and $[\text{Mo}^{\text{VI}}\text{O}_2(\text{bdt})_2]^{2-}$ (Figure 1A,C, bdt = benzene-1,2-dithiolate(2-)) that model the oxo atom transfer reaction of SO. These data are correlated to DFT calculations, and the calculations are used to evaluate oxo transfer from $\text{Mo}^{\text{VI}}\text{O}_2^{2-}$ to trimethylphosphite substrate. The nature of this reaction is then compared to our previous results¹⁰ on oxo transfer from DMSO to a Mo^{IV} dithiolene complex. This study provides new insight into these oxo transfer reactions, which are found to be fundamentally different. The DMSO reductase reaction involves a late transition state where oxo transfer leads to electron transfer, while the sulfite oxidase reaction has an early transition state with electron transfer inducing the oxo transfer. This study further considers the intrinsic barriers of both sets of structures for both reactions and is extended to consider the active site reactivity of SO.

2. EXPERIMENTAL SECTION

2.1. Sample Preparation. The $[\text{Mo}^{\text{IV}}\text{O}(\text{bdt})_2]^{2-}$ and $[\text{Mo}^{\text{VI}}\text{O}_2(\text{bdt})_2]^{2-}$ complexes were prepared as in the literature.²⁷

2.2. S K-Edge XAS Data Collection and Analysis. All sulfur K-edge XAS data were measured at the Stanford Synchrotron Radiation Lightsource (SSRL) using the 54-pole wiggler beamline 6-2 operating in high field mode of 10 kG with a Ni-coated harmonic rejection mirror and a fully tuned Si(111) crystal monochromator. Details of the beamline configuration are given in ref 25. The solid samples were ground into fine powders in an inert atmosphere (N_2) dry glovebox where the O_2 level was less than 1 ppm and dispersed as thinly as possible on Mylar tape to minimize potential self-absorption. A 6 μm -thick, sulfur-free polypropylene front window was used to prevent sample exposure to air upon mounting in the sample box. The photon energy was calibrated to the maximum of the first pre-edge feature of $\text{Na}_2\text{S}_2\text{O}_3 \cdot 5\text{H}_2\text{O}$ at 2472.02 eV. A total of 3–5 scans were measured for each sample to ensure reproducibility. Raw data were calibrated and averaged using MAVe in the EXAFSPAK software package.²⁸ With the use of the PySpline program,²⁹ the background was removed from all spectra by fitting a second-order polynomial to the pre-edge region and subtracting it from the entire spectrum. Normalization of the data was accomplished by fitting a flat second-order polynomial or straight line to the post-edge region and normalizing the edge jump to 1.0 at 2490.0 eV.²⁴ Since the post-edge region also contains intensity from the Mo L_3 -edge, the data were further scaled such that the region between the S K-edge and Mo L_3 -edge had the same intensity as the corresponding region of a tungsten dithiolene complex.¹⁰ The error from background subtraction and normalization is less than 1%. Intensities of the pre-edge features were obtained by fitting the spectra with peaks having pseudo-Voigt line shape peaks with 1:1 Lorentzian to Gaussian contributions, using the EDG_FIT program.²⁸ The reported intensity values were based on the average of 10–12 good fits. The intensities of the S $1s \rightarrow \text{C}-\text{S} \pi^*/\sigma^*$ transitions at ~ 2473.8 eV were based on previously published values for similar complexes,¹⁰ where these edge features were better resolved, allowing for $\pm 10\%$ variation of the intensities and peak widths. The error from the fitting procedure was less than 10%. The fitted intensities were converted to %S 3p character using eq 1, where D_0 is the peak area and the value of I_s was set at 14.1,¹⁰ the same as previously published results for similar complexes.

2.3. DFT Calculations. DFT calculations were performed using the Gaussian 09 package³⁰ with both the pure functional BP86 (Becke GGA exchange with Perdew 1986 nonlocal correlation^{31,32}) and the hybrid functional B3LYP (Becke GGA exchange including 20%

Hartree–Fock mixing and Lee, Yang, and Parr correlation effects³³), using the SDD basis set (triple- ζ quality with effective core potential) on the Mo atom,³⁴ 6-311G(d) basis set on the S, O, N and P atoms and 6-31G(d) on C and H atoms. Both functionals gave similar results, and only the B3LYP results are reported here (BP86 results given in Table S1). The geometry optimizations³⁵ were performed starting with the published crystal structures. Frequency calculations showed no imaginary frequencies for both reactants and products. All calculations used the polarized continuum model (PCM)³⁶ in acetonitrile. Mulliken populations and Mayer bond orders were obtained using the QMForge program, which makes extensive use of the cclib library.^{37,38} For reaction coordinate studies, intrinsic reaction coordinate (IRC) calculations were run after the frequency calculation at the transition state (only 1 imaginary frequency) to ensure that the pathway connects the transition state to both the reactant and product.

3. RESULTS AND ANALYSIS

3.1. Electronic Structures. 3.1.1. S K-Edge XAS Data. The sulfur K-edge XAS spectra for the monooxo Mo^{IV} and bisoxo Mo^{VI} bis-dithiolene complexes are shown in Figure 2. The spectra of the $[\text{Mo}^{\text{IV}}(\text{OSi})(\text{bdt})_2]^-$ and $[\text{Mo}^{\text{VI}}\text{O}(\text{OSi})(\text{bdt})_2]^-$ complexes are also included for reference. The $[\text{Mo}^{\text{IV}}\text{O}(\text{bdt})_2]^{2-}$ complex (Figure 2A) has a dominant feature at

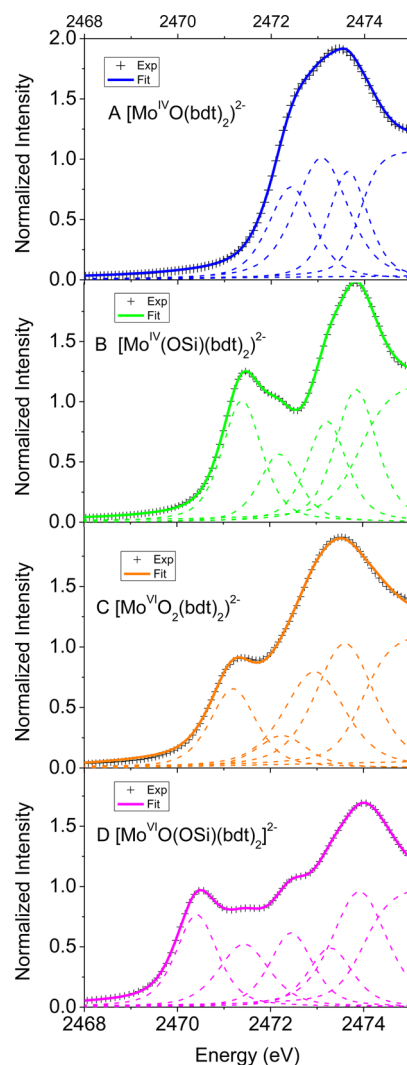


Figure 2. S K-edge XAS spectra of (A) $[\text{Mo}^{\text{IV}}\text{O}(\text{bdt})_2]^{2-}$, (B) $[\text{Mo}^{\text{IV}}(\text{OSi})(\text{bdt})_2]^-$, (C) $[\text{Mo}^{\text{VI}}\text{O}_2(\text{bdt})_2]^{2-}$, and (D) $[\text{Mo}^{\text{VI}}\text{O}(\text{OSi})(\text{bdt})_2]^-$.

Table 1. Experimental and Theoretical S Covalency in Mo Bis-dithiolene Complexes

complex	orbital	S K-edge XAS					DFT	
		E (eV)	D _o	h	S p (%)	RE (eV) ^a	S p (%)	RE (eV)
[Mo ^{IV} O(bdt) ₂] ²⁻	d _{xz} /d _{yz}	2472.4	1.12	4	38	0	31	0
	d _{xy} /d _z ²	2473.1	1.36	4	59	0.7	59	0.7
[Mo ^{IV} O ₂ (bdt) ₂] ²⁻	d _{yz} /d _y ² (O out of plane π+/π-)	2471.2	0.79	4	33	-1.3	31	-1.2
	d _x ² - _z ² (O in plane π+)	2472.2	0.67	2	15	-0.3	10	-0.3
	d _x ² - _y ² (O in plane σ+)	2473.0	1.02	2	53	0.6	38	0.6
	d _{xz} (O in plane σ-)	Not shown	NA	2	NA	NA	23	2.5

^aRE stands for Relative Energy. We use the lowest pre-edge energy in [Mo^{IV}O(bdt)₂]²⁻ as a reference.

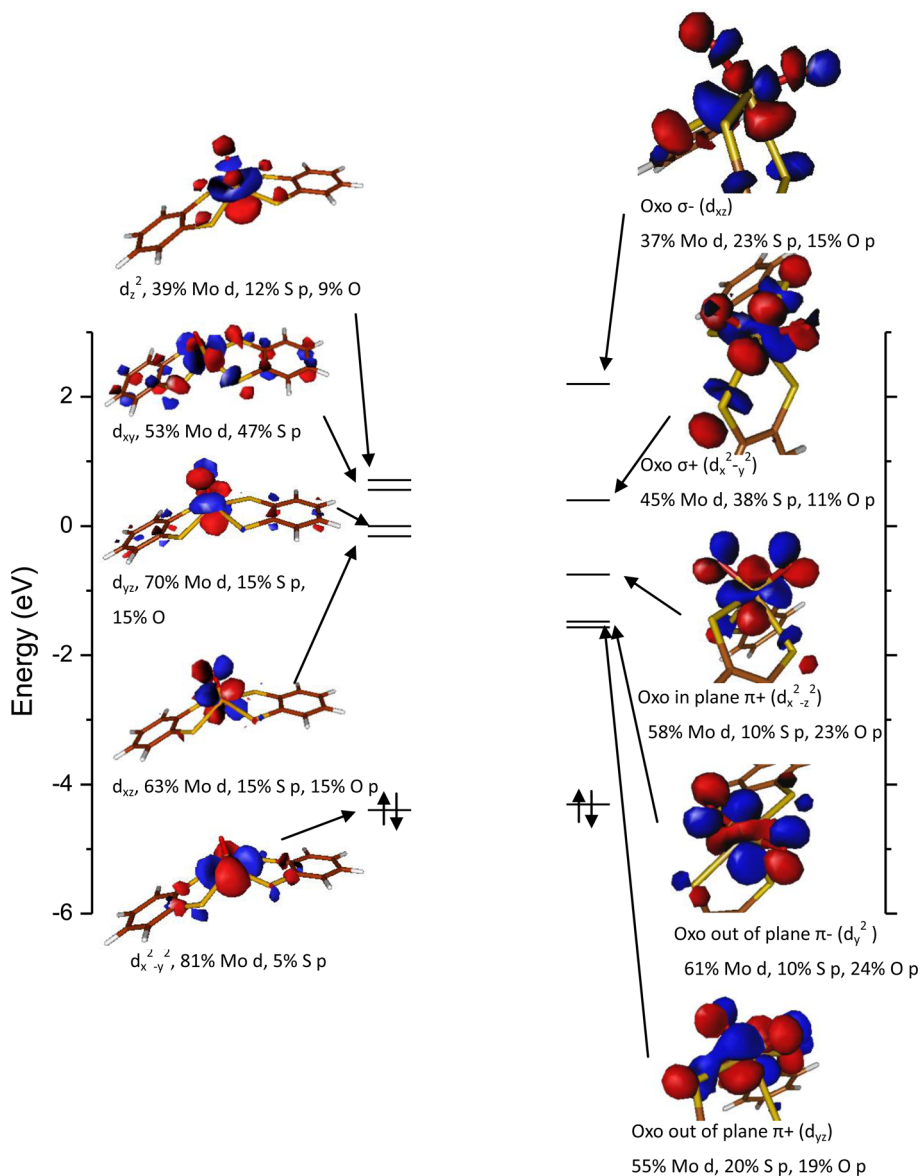


Figure 3. MO diagrams of [Mo^{IV}O(bdt)₂]²⁻ (left) and [Mo^{VI}O₂(bdt)₂]²⁻ (right). Selected atoms in [Mo^{VI}O₂(bdt)₂]²⁻ have been removed for clarity.

~2473.1 eV. There is also a low energy shoulder at ~2472.4 eV. On the basis of the second derivative of the spectrum (Figure S1A), there is an additional peak at ~2473.7 eV below the rising edge. Compared to the spectrum of the [Mo^{IV}(OSi)(bdt)₂]⁻ complex (Figure 2B), which requires a total of four peaks below the edge for a good fit, the three pre-edge features

in the [Mo^{IV}O(bdt)₂]²⁻ complex are shifted to higher energy due to the presence of the strong oxo ligand, which destabilizes the energies of the unoccupied Mo d orbitals.

The [Mo^{VI}O₂(bdt)₂]²⁻ complex (Figure 2C) has a dominant feature at ~2473.0 eV, and a clear pre-edge feature at ~2471.2 eV. From the second derivative (Figure S1B), there are two

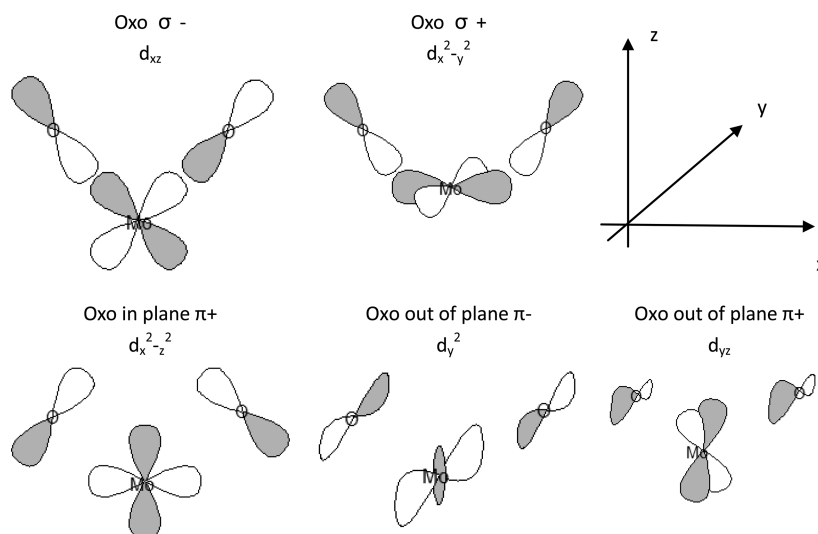


Figure 4. Symmetry adapted linear combinations (SALCs) of oxo $p\pi$ and $p\sigma$ orbitals and the d-orbital mixings in the antibonding MOs of bisoxo Mo^{VI} bis-dithiolene complex. The coordinate system is given in the upper right panel.

additional peaks required at ~ 2472.2 and ~ 2473.7 eV. Compared to the spectrum of the $[\text{Mo}^{\text{VI}}\text{O}(\text{OSi})(\text{bdt})_2]^-$ complex (Figure 2D), which requires five peaks below the edge for a good fit, all four pre-edge features are again shifted to higher energy due to the additional oxo ligand in the bisoxo Mo^{VI} complex.

In comparing the Mo^{VI} to the Mo^{IV} complexes, the pre-edge features for the $[\text{Mo}^{\text{VI}}\text{O}_2(\text{bdt})_2]^{2-}$ complex are at lower energy relative to those for the $[\text{Mo}^{\text{IV}}\text{O}(\text{bdt})_2]^{2-}$ complex. A similar low energy feature is also observed in the comparison of the $[\text{Mo}^{\text{VI}}\text{O}(\text{OSi})(\text{bdt})_2]^-$ and the $[\text{Mo}^{\text{IV}}(\text{OSi})(\text{bdt})_2]^-$ complexes. The lower pre-edge energy for the Mo^{VI} complexes is due to both the presence of an additional unoccupied d-orbital (2 spin holes) for the Mo^{VI} relative to the Mo^{IV} complexes, which corresponds to the lowest energy peak, and the increased Z_{eff} of Mo^{VI} , which shifts the d-manifold down in energy.

The energies and intensities obtained from the fits are given in Table 1. Peak assignments are presented below.

3.1.2. DFT Correlations to XAS Spectra. Spin-unrestricted DFT calculations were used for peak assignments and for quantitative comparisons to the experimental data. The fully optimized geometric structures are consistent with the crystal structures which have bond distances within 0.04 \AA , and bond angles within 3° (Figure 1).³⁹ Molecular orbital diagrams for the $[\text{Mo}^{\text{IV}}\text{O}(\text{bdt})_2]^{2-}$ and $[\text{Mo}^{\text{VI}}\text{O}_2(\text{bdt})_2]^{2-}$ complexes are presented in Figure 3. The MO contours for the reference compounds in Figure 1B,D are shown in Figure S2 for comparison.

In the five-coordinate, square pyramidal $[\text{Mo}^{\text{IV}}\text{O}(\text{bdt})_2]^{2-}$ complex, the $\text{Mo } d_{x^2-y^2}$ orbital is predominantly nonbonding and is the HOMO (z -axis along the Mo-oxo bond, and x -axis bisects the dithiolene ligands). There is a large HOMO/LUMO gap of 4.1 eV . The LUMO is close to the nearly degenerate $\text{Mo } d_{xz}/d_{yz}$ set, which is strongly π -antibonding to both the oxo atom and dithiolene ligands (i.e., contains significant S p character), thus the low energy peak at $\sim 2472.5 \text{ eV}$ in Figure 2A is assigned as the $\text{S } 1s \rightarrow \text{Mo } d_{xz}/d_{yz}$ transitions. The calculated total S $3p$ character in these two MOs is 31% , while experimentally, the S pre-edge intensity gives 38% . The $\text{Mo } d_z^2$ and $\text{Mo } d_{xy}$ orbitals are σ antibonding to the ligands and thus at higher energies. On the basis of the calculation shown in

Figure 3A, the $\sim 2473.3 \text{ eV}$ peak is assigned as the $\text{S } 1s \rightarrow \text{Mo } d_{xy}/d_z^2$ transitions. The total S $3p$ covalency is 59% both experimentally and computationally. In the $[\text{Mo}^{\text{IV}}(\text{OSi})(\text{bdt})_2]^-$ reference complex, d_z^2 and d_{xy} are well separated in energy with the d_{xy} at higher energy by $\sim 1 \text{ eV}$ (see figure S2). In the $[\text{Mo}^{\text{IV}}\text{O}(\text{bdt})_2]^{2-}$ complex, the d_z^2 is shifted to higher energy, close to d_{xy} due to the strong axial Mo-oxo bond. From our previous studies on the Ni and Mo bis-dithiolene complexes, the $\sim 2473.7 \text{ eV}$ peak in Figure 2A is assigned as the $\text{S } 1s \rightarrow \text{C-S } \pi^*/\sigma^*$ intradithiolene ligand transitions.^{40,41}

As shown in Figure 4, for the six-coordinate $[\text{Mo}^{\text{VI}}\text{O}_2(\text{bdt})_2]^{2-}$ complex, the z -axis is defined as bisecting the O–Mo–O angle, the x -axis is perpendicular to z and in the O–Mo–O plane, and the y -axis is perpendicular to this plane. For this cis bisoxo Mo complex, the energies of the Mo d -orbitals are dominated by their σ/π bonding interactions with the two strong oxo donor ligands. The six $2p$ -orbitals on the 2 oxo atoms form six combinations: the out of plane $\pi+$ and $\pi-$, in-plane $\pi+$ and $\pi-$, and $\sigma+$, $\sigma-$; π indicates perpendicular to the O–Mo–O plane while σ indicates along the bond, and the $+/-$ subscripts indicate the symmetric and antisymmetric combinations of the specific O $2p$ -orbitals. The in-plane $\pi-$ is nonbonding. The out-of-plane $\pi+$ and $\pi-$, and in-plane $\pi+$ interact with the $d\pi$ orbitals on Mo, with the in-plane $\pi+$ interaction being the strongest due to its increased overlap with the $\text{Mo } (d_x^2-z^2)$ (see Figure 3). Thus, the low energy peak at $\sim 2471.2 \text{ eV}$ in Figure 2C is assigned as the combined set of transitions from the $\text{S } 1s \rightarrow \text{Mo } d_{yz}$ (that interacts with the out-of-plane oxo $\pi+$) and the $\text{S } 1s \rightarrow \text{Mo } (d_y^2)$ (that interacts with the out-of-plane oxo $\pi-$). Experiment gives 33% S p character, while the DFT calculation has a total of 31% S $3p$ character in these two transitions. The peak at 2472.2 eV , which is $\sim 1 \text{ eV}$ to higher energy, is assigned as $\text{S } 1s \rightarrow \text{Mo } (d_x^2-z^2)$ (that interacts with in-plane oxo $\pi+$) transition. Experimentally, this transition has 15% S $3p$ character, while the calculation gives 10% .

The MOs with oxo σ character are strongly antibonding and thus at higher energy. The $\sim 2473.0 \text{ eV}$ peak is assigned as the $\text{S } 1s \rightarrow \text{Mo } (d_x^2-d_y^2)$ (antibonding with oxo atoms $\sigma+$). The S covalency is 53% from calculation vs 38% from experiment. The $\text{S } 1s \rightarrow \text{Mo } (d_{xz})$ (antibonding with oxo atoms $\sigma-$) transition is calculated to be $\sim 3.8 \text{ eV}$ above the LUMO,

overlapping the rising edge and thus could not be experimentally resolved. Computationally, this transition has 23% S p character. Finally, on the basis of our previous studies⁵, the ~2473.6 eV peak is assigned as S 1s → C–S π^*/σ^* intra-dithiolene ligand transitions.

Comparisons of the DFT calculations with S K-edge XAS experimental data show that the calculations reproduce the pre-edge transition energy splittings, but somewhat underestimate the S covalency (Table 1). However, these DFT calculations did well in reproducing the experimental energies and intensities in the lower energy region. As the low-energy unoccupied MOs are the frontier molecular orbitals (FMO) in the oxo transfer reaction, these DFT calculations will be used to further evaluate the reaction coordinate for oxo transfer to phosphite ester (Section 3.3).

In comparing the $[\text{Mo}^{\text{IV}}\text{O}(\text{bdt})_2]^{2-}$ to the $[\text{Mo}^{\text{VI}}\text{O}_2(\text{bdt})_2]^{2-}$ complexes, the total S experimental covalency changes from 194% to 248%, an increase of 54%, (computationally 180% to 204%, an increase of 24%). This increase is much smaller than the increase observed for the tris-dithiolene Mo^{IV} and Mo^{VI} complexes⁴⁰ (118%), which undergo a ligand-based redox process (i.e., noninnocent behavior). Thus, for the monooxo Mo^{IV} and bisoxo Mo^{VI} complexes, the presence of oxo ligands leads to innocent behavior of the dithiolenes where the covalent donor bonding to the Mo simply increases upon oxidation of the metal center.

3.2. Oxo Bond Strengths. The DFT calculations were further used to estimate the Mo^{VI} -oxo bond strengths in the bisoxo and monooxo complexes and to compare to experimental values where available. These values are necessary for consideration of the reaction coordinate results in the next section.

For the oxo transfer reaction: $\text{X} + 1/2\text{O}_2 \rightarrow \text{XO}$, the $\text{X}=\text{O}$ bond strength is the difference between one-half the O_2 bond strength and the ΔH of the reaction. The ΔH^{rxn} values were obtained from the DFT calculations, using 119 kcal/mol for the value of the O_2 bond strength.^{42–44} These oxo bond strengths are given in Table 2. The computational results are within 7 kcal/mol of the experimental values, where available.^{42–45}

The Mo–oxo bond strength in $[\text{Mo}^{\text{VI}}\text{O}_2(\text{bdt})_2]^{2-}$ is ~104 kcal/mol, while that in $[\text{Mo}^{\text{VI}}\text{O}(\text{OSi})(\text{bdt})_2]^-$ is ~118 kcal/mol. Thus, the monooxo compound has a 14 kcal/mol stronger Mo–oxo bond, out of ~118 kcal/mol. From the energy diagram in Figure 3, the Mo^{IV} –oxo bond order in the monooxo complex is 3, which will remain the same in the Mo^{VI} monooxo complex (i.e., 2 electrons are lost from the nonbonding d_{xy} orbital), while the Mo–oxo bond order in the Mo^{VI} bisoxo complex is 2.5 per bond. On breaking the Mo–oxo bond in the monooxo complex, the bond order of 3 is lost. Alternatively, breaking one Mo–oxo bond in the bisoxo complex generates a monooxo product which has a Mo–oxo bond order of 3; thus, the bond order only decreases by 2. This reflects the spectator oxo effect described by Rappe and Goddard.⁴⁶

This ~10% decrease in bond strength can be considered quantitatively in terms of the Mayer bond orders (MBO)⁴⁷ acquired from the DFT calculations. In the $[\text{Mo}^{\text{VI}}\text{O}_2(\text{bdt})_2]^{2-}$ compound, the MBO for each Mo–oxo bond is 1.81, and in the $[\text{Mo}^{\text{IV}}\text{O}(\text{bdt})_2]^{2-}$ compound, the Mo–oxo MBO is 1.99. Loss of one oxo ligand from the $[\text{Mo}^{\text{VI}}\text{O}_2(\text{bdt})_2]^{2-}$ complex to produce the $[\text{Mo}^{\text{IV}}\text{O}(\text{bdt})_2]^{2-}$ complex eliminates a MBO contribution of 1.81, while the remaining spectator Mo–oxo MBO increases from 1.81 to 1.99; thus, the total Mo–oxo MBO lost is 1.63 ($1.99 - 1.81 \times 2$). In the $[\text{Mo}^{\text{VI}}\text{O}(\text{OSi})-$

Table 2. Comparative Experimental and Computational Oxo Bond Energies

compound	oxo bond	experimental bond strength (kcal/mol)	computational bond strength (kcal/mol) ^a
O_2	$\text{O}=\text{O}$	119	–
DMSO	$\text{S}=\text{O}$	87	91
$\text{O}=\text{P}(\text{Me})_3$	$\text{P}=\text{O}$	139	144
$\text{O}=\text{P}(\text{Pr})_3$	$\text{P}=\text{O}$	138	144
$\text{O}=\text{P}(\text{Bu})_3$	$\text{P}=\text{O}$	137	144
$\text{O}=\text{P}(\text{OMe})_3$	$\text{P}=\text{O}$		151
$\text{O}=\text{P}(\text{OEt})_3$	$\text{P}=\text{O}$	150	151
SO_4^{2-}	$\text{S}=\text{O}$		146
HSO_4^-	$\text{S}=\text{O}$	123	122
H_2SO_4	$\text{S}=\text{O}$		107
$[\text{Mo}^{\text{VI}}\text{O}_2(\text{bdt})_2]^{2-}$	$\text{Mo}=\text{O}$		104
$[\text{Mo}^{\text{VI}}\text{O}_2(\text{mdt})_2]^{2-}$	$\text{Mo}=\text{O}$		106
$[\text{Mo}^{\text{VI}}\text{O}_2(\text{mnt})_2]^{2-}$	$\text{Mo}=\text{O}$		102
$[\text{Mo}^{\text{VI}}\text{O}(\text{OMe})(\text{bdt})_2]^-$	$\text{Mo}=\text{O}$		116
$[\text{Mo}^{\text{VI}}\text{O}(\text{OSi})(\text{bdt})_2]^-$	$\text{Mo}=\text{O}$		118
$[\text{Mo}^{\text{VI}}\text{O}_2(\text{mnt})(\text{SMe})]^-$	$\text{Mo}=\text{O}$		126

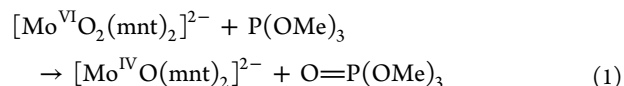
^aDFT calculations were carried out in Gaussian 09, using B3LYP functional, SDD basis set for Mo, 6-311G(d) for S, O, N and P, and 6-311G(d) for other atoms.

$(\text{bdt})_2]^-$ compound, the Mo–oxo MBO is 1.86 and in going to $[\text{Mo}^{\text{IV}}\text{O}(\text{OSi})(\text{bdt})_2]^-$, this MBO is lost. The ~13% decrease in Mo–oxo MBO lost in going from the bis- to monooxo, relative to mono- to desoxo conversion (both involving changing from a six-coordinate Mo^{VI} to a five-coordinate Mo^{IV}), is consistent with the ~10% Mo–oxo bond strength decrease, and reflects the effect of the spectator oxo in the bisoxo complex and its change in going to the monooxo Mo^{IV} complex.

3.3. Reaction Coordinates for Oxo Transfer.

3.3.1. Transfer to Phosphite Ester. In this section, we evaluate the oxo transfer process computationally using the Mo complexes with mnt ligands instead of bdt, because detailed kinetic data are available for oxo transfer from the $[\text{Mo}^{\text{VI}}\text{O}_2(\text{mnt})_2]^{2-}$ complex to $\text{P}(\text{OR})_3$.²³ As described in Table S2, the geometric and electronic structures of the $[\text{Mo}^{\text{VI}}\text{O}_2(\text{mnt})_2]^{2-}$ and $[\text{Mo}^{\text{IV}}\text{O}(\text{mnt})_2]^{2-}$ complexes are very similar to those of the analogous bdt ligand complexes studied above.

For the oxo transfer reaction:



the calculated ΔH^{rxn} is –49 kcal/mol (Figure 5A, R → P), which reflects the difference in the $\text{X}=\text{O}$ bond strengths of $[\text{Mo}^{\text{VI}}\text{O}_2(\text{mnt})_2]^{2-}$ and $\text{O}=\text{P}(\text{OMe})_3$ (151–102 kcal/mol, Table 2).

Three possible transition states were found for reaction 1 (Figure 5A). Each transition state structure in Figure 5A has only one imaginary frequency, and has an intrinsic reaction coordinate (IRC, a one-dimensional path along the potential energy curve of a chemical reaction which describes the path of least resistance between reactants and products) coupling it to both the reactant and product. TS1 has the phosphite ester P bonding to one of the terminal oxo atoms. It is very similar to that described elsewhere.⁴⁸ TS2 has the phosphorus atom bound to both oxo atoms to form a bis(μ -oxo) structure. TS3 is similar to TS1, but with a different P–O orientation, such that

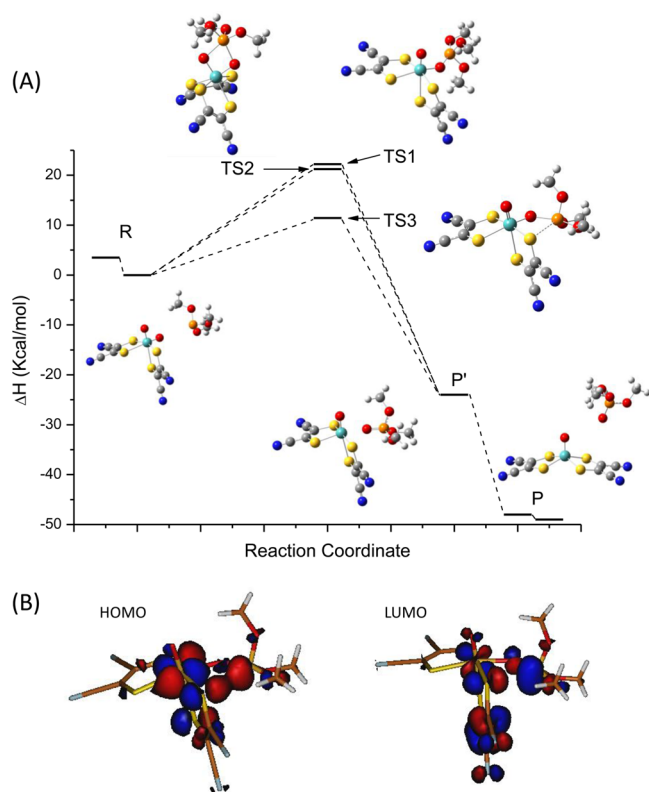


Figure 5. (A) Geometric structures and enthalpies at different stages of the reaction coordinate of (1). R for Reactant, TS for Transition State, P' for the state on the path way that the oxo has been transferred while the product is still bound, P for Product. (B) HOMO (left) and LUMO (right) around TS3, showing the bonding/antibonding interaction between the phosphorus lone pair and $d\pi$ oxo as well as one of the dithiolene sulfurs.

the phosphorus atom also interacts with one of the sulfurs of a dithiolene ligand. The P–O orientation in TS3 is similar to a known structure,¹⁸ but the compound in that study does not have delocalized dithiolene ligation. TS3 has the lowest energy barrier (12 kcal/mol; TS1 has 21 and TS2 has 20 kcal/mol), which is very similar to the ΔH^\ddagger that was measured experimentally (10 kcal/mol).²³

There are two major points to note about the geometric and electronic structures of these transition states. First, TS3 has a P–S interaction involving the phosphorus lone pair donating electron density into the Mo-based unoccupied d-orbital that is delocalized onto the oxo and the S p orbital that is perpendicular to the dithiolene plane (Figure 5B). The P–S distance is ~ 3.3 Å and the P–S MBO is 0.15. This P–S interaction stabilizes the transition state by ~ 10 kcal/mol relative to TS1, which has the P lone pair interact only with the oxo $p\pi$ orbital. Second, one of the O(Me)–P–O(Mo) angles in TS3 (and TS1) is almost linear ($\sim 165^\circ$). This was first noted by Hall and colleagues,¹⁸ and attributed to a nucleophilic attack of the occupied oxo p orbital on the σ^* orbital of the phosphite ester. From a fragment analysis, at the transition state, there is about $\sim 1.5\%$ phosphite ester σ^* character mixed into the occupied valence orbitals. This mixing is only observed around the transition state, and can be eliminated by decreasing the O(Me)–P–O(Mo) angle. This results in an ~ 4 kcal/mol energy penalty. Alternatively, there is $\sim 17\%$ of the phosphite ester lone pair orbital mixed into the unoccupied valence d orbital at the transition state (Figure 5B LUMO). Thus, the

electron transfer accompanying the oxo transfer process is mainly the phosphorus lone pair into the empty Mo d π orbital through the oxo bridge.

At TS3 in Figure 5A, the Mo–O distance is 1.83 Å and the P–O distance is 1.99 Å, while the Mo–O distance for the $[\text{Mo}^{\text{VI}}\text{O}_2(\text{mnt})_2]^{2-}$ reactant is 1.72 Å, and the P–O distance for the $\text{O}=\text{P}(\text{OMe})_3$ product is 1.48 Å. Thus, the Pauling bond fraction⁴⁹ for the Mo–O bond is 1.43 (decreased from 2.11), and that of the P–O bond is 0.33. Figure 6A gives this in terms

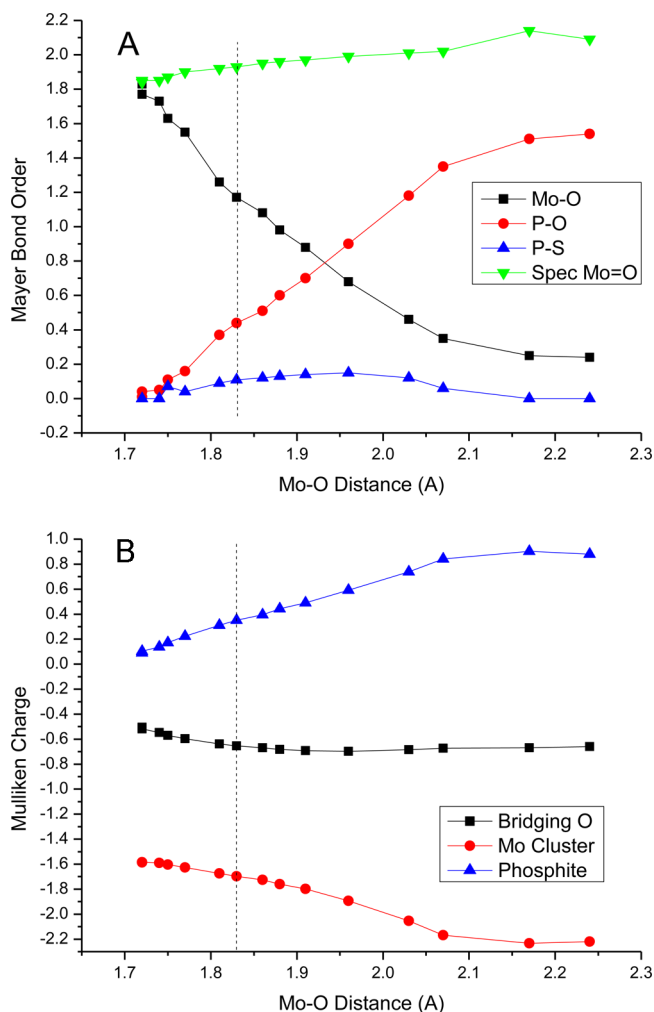


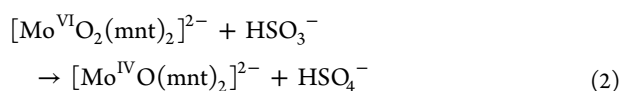
Figure 6. Mayer bond order (MBO) (A) and Mulliken charge change (B) for reaction 1 along the reaction coordinate in terms of Mo–O distance. Spec Mo=O indicating the spectator oxo in $[\text{Mo}^{\text{VI}}\text{O}_2(\text{mnt})_2]^{2-}$, which is the oxo atom that is not transferred. The dashed line indicates the distance in TS3.

of Mayer bond orders at the transition state: $\sim 1/3$ of the Mo–O bond order is lost (a decrease in MBO from 1.84 to 1.17) and $\sim 1/4$ of the P–O bond is formed (an increase from 0.00 to 0.43; the MBO for the $\text{P}=\text{O}$ bond in the product is 1.80). Figure 6B shows that about $1/3$ of the charge has been transferred from the substrate to the Mo complex at this transition state. The above results indicate that this oxo transfer reaction has an early transition state, with only 0.1 Å of Mo–O bond elongation.

The calculations show that there is not much structural rearrangement of the dithiolenes and the spectator oxo atom in this oxo transfer reaction. When this oxo transfer is complete,

but with the phosphate ester product still bound (P' in Figure 5A, which was obtained from a point on the IRC toward the product with a Mo–O(phosphite ester) bond distance of 2.24 Å), the two dithiolene planes remain perpendicular to each other, as in R and TS3. However, P' is not a local minimum, and the product is lost along the reaction coordinate to give the monooxo Mo^{IV} complex. As the phosphate ester comes off, the two dithiolenes rotate into the same plane to form P (Figure 5A), and the enthalpy is lowered by 25 kcal/mol from P' to P. This is in contrast to the reaction coordinate in refs 18 and 20, where the product remained bound. This difference reflects the fact that the final product in reaction 1 is a five-coordinate [Mo^{IV}O(mnt)₂]²⁻ complex that has its two dithiolenes coplanar. The four S pπ orbitals that are perpendicular to the dithiolene planes are parallel with each other, and this stabilizes the square pyramidal five-coordinate Mo monooxo complex.

3.3.2. Transfer to Sulfite. Sarkar et al. found that the [Mo^{VI}O₂(mnt)₂]²⁻ complex can also transfer an oxo atom to bisulfite,¹⁷ which is the native substrate of sulfite oxidase, to form bisulfate. They showed that the reaction

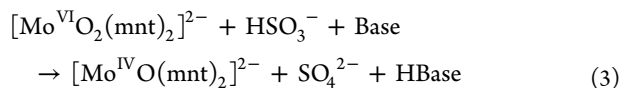


exhibits Michaelis–Menten kinetics. However, the proposed transition state has an oxo atom of the substrate bound to the Mo to form a seven-coordinate structure, and is too high in energy (36 kcal/mol) for reaction 2 to occur based on kinetic data.⁵⁰ It is also not on the IRC. A lower energy transition state was thus found, and determined to be on the IRC to both the reactant and the product. This transition state is very similar to TS3 in Figure 5A with the sulfur atom of HSO₃⁻ bound to one of the terminal oxo atoms (Figure S3).

Note that an ES precursor complex is obtained from the IRC (Figure S3) that has the HSO₃⁻ anion bound to the [Mo^{VI}O₂(mnt)₂]²⁻ complex through an H-bond to one of the dithiolene sulfurs. This is consistent with the observation that reaction 2 with a monoprotonated sulfite exhibits Michaelis–Menten kinetics, while reaction 1 with phosphite ester is second-order.

The calculated ΔH[‡] for reaction 2 is 23 kcal/mol, and the intrinsic barrier (obtained by using the Marcus equation^{51,52} to eliminate the effect of the thermodynamic driving force) is 32 kcal/mol. This is similar to the intrinsic barrier of reaction 1 (28 kcal/mol); thus, the difference in barrier heights between reactions 1 and 2 simply reflects the difference between the X=O bond strengths in the product (151 kcal/mol for phosphate ester vs 122 kcal/mol for bisulfate).

A second-order rate constant for reaction 2 (at low substrate concentration, before saturation) of ~60 M⁻¹ s⁻¹ has been reported.¹⁷ This value is 3 orders of magnitude faster than that observed for reaction 1 at the same temperature (1.7 × 10⁻² M⁻¹ s⁻¹), which is not consistent with the difference in the product bond strengths. Reaction 2 was performed at pH ~ 5 (the Mo compound is not stable under basic conditions). At pH 5, the reactant is monoprotonated HSO₃⁻ (pK_a = 7.2); however, the product should be deprotonated SO₄²⁻ (pK_a = 1.9). Thus, the reaction measured experimentally is



Thermodynamically, the S=O bond in SO₄²⁻ is ~20 kcal/mol stronger than that in HSO₄⁻; thus, the free energy for the formation of SO₄²⁻ is larger. Computationally, the ΔG[‡] for reaction 2 is 27 kcal/mol, and the ΔG[‡] for the reaction [Mo^{VI}O₂(mnt)₂]²⁻ + SO₃²⁻ → [Mo^{IV}O(mnt)₂]²⁻ + SO₄²⁻ is 3 kcal/mol. Experimentally, the ΔG[‡] for reaction 3 is ~13 kcal/mol based on the kinetics data (1.7 × 10⁻² M⁻¹ s⁻¹ at 298 K at low concentration).

The conjugate base of propionic acid was used to model the protonation behavior of bisulfite and sulfate in solution, such that bisulfite remain monoprotonated and sulfate is totally deprotonated. This was included next to the Mo complex as a base and the reaction coordinate with HSO₃⁻ was calculated as given in Figure 7.

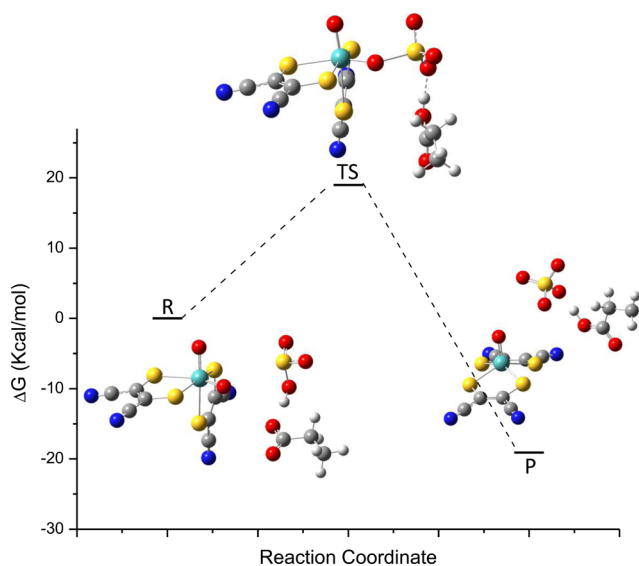


Figure 7. Reaction coordinate of reaction 3. The conjugate base of propionic acid was used to model the protonation behavior of bisulfite and sulfate in solution.

The substrate HSO₃⁻ is almost deprotonated at the transition state, with an O–H MBO of 0.16 to the substrate, and 0.59 to the base. The calculated ΔG[‡] for this reaction is 19 kcal/mol, which is reasonably consistent with experimental data. Thus, loss of the proton from the substrate occurs at an early stage and facilitates the oxo transfer reaction to sulfite.

4. DISCUSSION

4.1. Nature of the Oxo Transfer Reaction to Phosphite Ester. The S K-edge XAS and DFT results show that the transformation from [Mo^{VI}O₂(bdt)₂]²⁻ to [Mo^{IV}O(bdt)₂]²⁻ involves a metal-based redox process; thus, the dithiolenes act as innocent covalent ligands in the oxo transfer reaction. It is initiated by the phosphorus lone pair attack on an unoccupied metal-based dx^z-orbital that contains oxygen pπ character, which leads to the formation of the P–O bond and loss of the Mo–oxo bond. The almost linear R–P–O bond angle¹⁸ and a P–S interaction between the phosphite and a dithiolene ligand (see Figure 5) help stabilize the TS structure. On the basis of Mulliken charges and Mayer bond orders (Figure 6), about 1/3 of the oxo bond from the Mo and the electron pair from the phosphite ester are transferred at the TS, while the Mo–O bond has only been elongated by 0.1 Å. The two dithiolene planes remain almost perpendicular throughout the oxo transfer

process, and subsequently, there is an additional ~ 25 kcal/mol driving force for the two dithiolenes to reorient into the five-coordinate square pyramidal monooxo Mo^{IV} product where the dithiolenes are now coplanar and the product is released (Figure 5A). The ~ 25 kcal/mol driving force is consistent with the fact that the phosphate ester product does not remain bound to the Mo^{IV} O bis-dithiolene complex, in contrast to nondithiolene Mo systems where the product remains bound after oxo transfer.

4.2. Comparison of Oxo Transfer from a Metal-Oxo to Substrate versus Oxo Transfer from a Substrate Oxo to Metal Ion. From a comparison to our previous study,⁵³ there is a major difference in the TS for oxo transfer from substrates to desoxo Mo^{IV} complexes, relative to oxo transfer from bisoxo Mo^{VI} complexes to substrates. In the former, the electron transfers from the occupied d-orbital of Mo^{IV} to the substrate $\text{X}-\text{O} \sigma^*$ orbital. The energy gap between the two FMOs in the reactants (the Mo d HOMO and the $\text{O}=\text{S} \sigma^*$ substrate LUMO) is ~ 6 eV (Figure 8 top). The substrate $\text{S}=\text{O}$ bond must greatly elongate to bring down the energy of the substrate σ^* orbital to interact with the Mo d HOMO, and polarize the $\text{S}=\text{O}$ bond to allow this electron transfer at a closer energy gap and with better overlap of the FMOs (Figure 8 top). Thus, the TS is late in $\text{S}-\text{O}$ bond elongation, and for the DMSO

reductase reaction, it is oxo atom transfer from the substrate that initiates the electron transfer from the Mo center.

For the reaction coordinate involving oxo transfer from bisoxo Mo^{VI} to a phosphite substrate, in analogy to the sulfate oxidase enzyme reaction, electrons are transferred from the phosphorus lone pair into the low energy unoccupied Mo d-orbital. This LUMO is a $d\pi$ orbital with oxo $p\pi$ character, with a calculated energy gap between the FMOs in the reactants of ~ 4 eV (Figure 8 bottom). This low energy splitting allows orbital mixing and thus electron transfer, from the substrate HOMO into the LUMO of the oxo Mo complex. Also, the oxo $p\pi$ character of the Mo d-acceptor is large enough to overlap with the phosphorus lone pair with little additional polarization. Thus, the TS is early in $\text{Mo}-\text{O}$ coordinate, and in this case, it is the transfer of an electron pair from the phosphite ester that induces cleavage of the $\text{Mo}-\text{O}$ bond.

In general, when an oxo atom is transferred from a metal center to a substrate, an unoccupied d-orbital is involved which is close in energy to the substrate lone pair, allowing electron transfer. Relatively, when an organic oxo atom is transferred, the electron transfer is to the substrate-oxo σ^* orbital. The σ^* orbital is in general high in energy and has little oxo character due to the high electronegativity of O atom. Thus, the substrate oxo bond needs significant elongation to lower its energy and polarize to initiate the electron transfer.

4.3. Directionality. From thermodynamic considerations, the direction of these reactions is in part determined by the difference in oxo bond strengths (Table 2). Here, we use mdt ($\text{mdt} = 1,2\text{-dimethylethene-1,2-dithiolate}(2-)$) ligation to be consistent with our previously published results for DMSO reductase reactions. It is shown in Table S2 that Mo mdt complexes have geometric and electronic structures similar to those of the Mo bdt complexes. For the phosphite oxidation reaction, the $\text{P}=\text{O}$ bond strength is ~ 150 kcal/mol, while the $\text{Mo}-\text{oxo}$ bond in the Mo^{VI} bisoxo complex is 106 kcal/mol (Table 2). This large difference in oxo bond strength drives the oxo transfer to the phosphite. In the DMSO reductase reaction, the $\text{S}=\text{O}$ bond is 91 kcal/mol, while formation of mono $\text{Mo}^{\text{VI}}-\text{oxo}$ bond gives 116 kcal/mol; thus, it is energetically favorable to transfer the oxo from DMSO to the Mo center.

However, there are also kinetic considerations in the directionality of oxo transfer. In comparing the bisoxo Mo^{VI} and the monooxo Mo^{VI} complexes in the reaction involving oxo transfer to phosphite, the difference in the reaction enthalpy is 9 kcal/mol, which reflects the bond strength difference (section 3.2). Their difference in the activation enthalpy is 3 kcal/mol (Figure S4), which gives an intrinsic barrier difference of only 1 kcal/mol. Both reactions are initiated by the phosphorus lone pair attacking the well-exposed oxo atom in the six-coordinate Mo^{VI} complexes, and the structures of their TS's are very similar. The distortion of the Mo complexes into five-coordinate products occurs after the TS. Electronically, both complexes use similar $d\pi^*$ FMOs with similar energy gaps (~ 4 eV in the reactant) and have similar phosphorus lone pair mixing into the Mo d LUMO ($\sim 30\%$) at the TS. Thus, oxo transfers from both bisoxo and monooxo Mo^{VI} to phosphite have very similar reaction coordinates with a rate difference reflecting their difference in reaction energy.

Alternatively, it is also thermodynamically favorable to transfer an oxo atom from DMSO to both the des- and monooxo Mo^{IV} complexes to form monooxo and bisoxo Mo^{VI} complexes, respectively, with the same 9 kcal/mol difference. However, the difference in enthalpic barrier height, ΔH^\ddagger , is 14

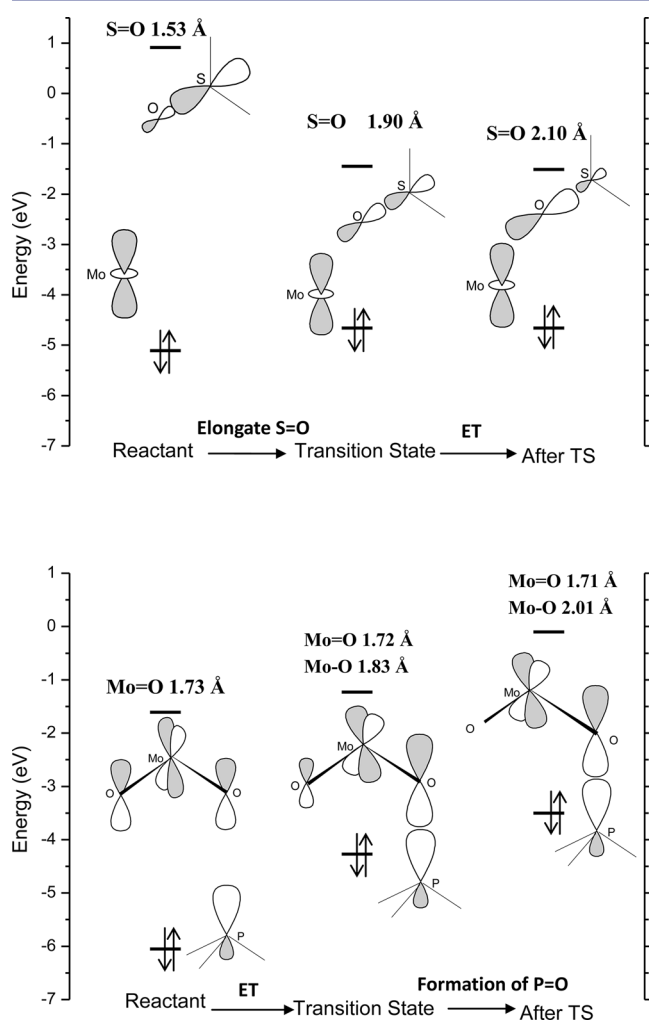


Figure 8. FMOs for DMSO oxo transfer to desoxo Mo^{IV} (top), and bisoxo Mo^{VI} oxo transfer to phosphine (bottom).

kcal/mol (Figure 9A, black vs green). This gives an intrinsic barrier for the monooxo to bisoxo reaction that is 9 kcal/mol higher than that for the des-to-mono oxo reaction.

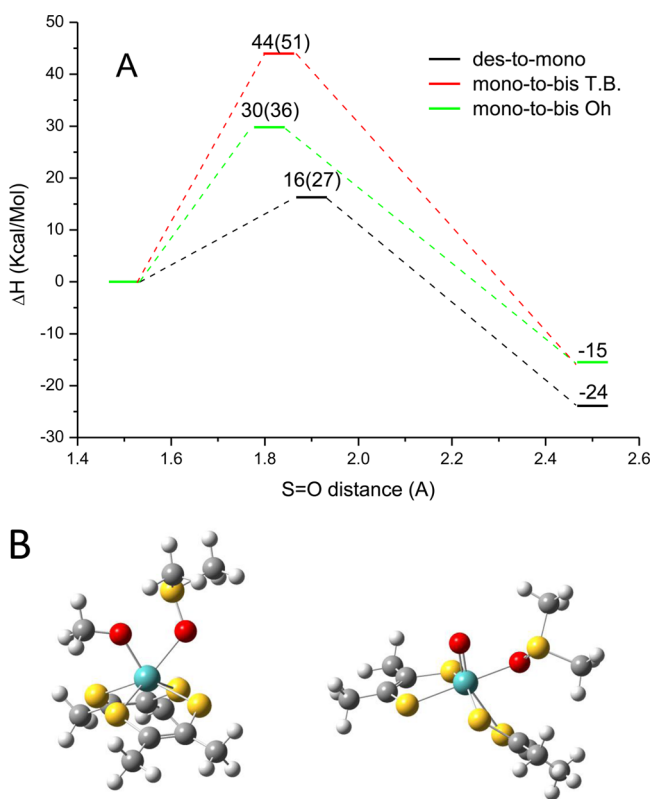


Figure 9. (A) Reaction coordinate for oxo transfer from DMSO to Mo^{IV} complexes. Enthalpic barriers and intrinsic barriers (in parentheses) are indicated. T.B. stands for trigonal bipyramidal. The TS in red has a similar geometry to the TS in black. The starting point is where the Mo complex and the DMSO are ~ 4 Å away from each other. (B) Geometry of the DMSO bound intermediate structure for the des-to-mono oxo (left) and mono-to-bis oxo (right) coordinate. Mo–O(DMSO) distance is constrained at 2.24 Å.

In the des-to-mono reaction, the reactant is a 5C Mo^{IV} complex. The methoxyl group distorts to open a site for DMSO to bind to form a 6C intermediate state (Figure 9B left). In this intermediate, DMSO-bound complex, the DMSO distortion energy is 3 kcal/mol, and the distortion energy of the Mo^{IV} desoxo complex is 18 kcal/mol. There is 12 kcal/mol interaction energy between the two fragments, due to 14%

donor and 2% backbonding interaction. Thus, the total energy of this DMSO bound state is 9 kcal/mol higher than that of the reactant, and there is an additional 7 kcal/mol required to reach the TS. In the mono-to-bis reaction, the five-coordinate Mo^{IV} complex does not distort as described above, because of the higher energy required to distort the strong oxo bond (see trigonal bipyramidal (TB) TS in Figure 9A red). Instead, the dithiolene planes rotate to leave an open position for DMSO binding (Figure 9B right). The DMSO distortion energy is similar (2 kcal/mol), but the bis-dithiolene- Mo^{IV} -oxo distortion energy is larger than that for DMSO binding to the desoxo Mo^{IV} (23 kcal/mol). There is also a decreased interaction energy (7 kcal/mol) reflecting decreased donor bonding of the DMSO to Mo^{IV} (8%) due to the strong oxo– Mo^{IV} bond. This leads to a higher total energy (18 kcal/mol) to bind DMSO to the $\text{Mo}^{\text{IV}}=\text{O}$ complex, and another 12 kcal/mol is required to reach the transition state.

In summary, for oxo transfer from six-coordinate Mo^{VI} complexes to phosphite, electron transfer leads to oxo transfer. The electron density in the phosphorus lone pair orbital readily interacts with the oxo p-character in the low energy unoccupied metal d-orbital; thus, both the bis-to-mono or mono-to-des reactions are accessible. Alternately, for oxo transfer from DMSO to the five-coordinate Mo^{IV} complexes, it is the oxo transfer that leads to electron transfer. This requires DMSO binding to the Mo^{IV} complex, which is more difficult in the presence of a strong oxo donor ligand.

4.4. Correlations to the Enzymes. With the results of the model studies, calculations can be used to consider the oxo transfer mechanism for native sulfite oxidase. Note that the substrate for the native enzyme is the fully deprotonated sulfite,⁵⁴ while the model complex in section 3.3.2 was not stable at the pH ~ 8 where SO_3^{2-} dominates. By systematically varying the substrate and the ligation of the Mo site, the results from the $[\text{Mo}^{\text{VI}}\text{O}_2(\text{mnt})_2]^{2-}$ complex can be extended to the enzyme active site (reaction numbers below correspond to those in Table 3).

Comparison of reactions (1) and (4) shows that for the same six-coordinate $[\text{Mo}^{\text{VI}}\text{O}_2(\text{mnt})_2]^{2-}$ complex, oxo transfer to SO_3^{2-} has a much lower barrier than to phosphite. The dianionic SO_3^{2-} has more charge density, thus its lone pair donor HOMO is closer in energy to the LUMO of the Mo bisoxo complex. Thus, even less distortion is required for the overlap of the FMOs for the electron transfer to induce oxo transfer to sulfite and there is an even earlier transition state (Table 3, shorter Mo–O distance and higher Mo–O bond order).

Table 3. Computational Comparison of Oxo Transfer from $\text{Mo}^{\text{VI}}\text{O}$ Dithiolene Complex to Two Different Substrates

rxn no.	Mo^{VI} site	substrate	ΔH^{ran} (kcal/mol)	ΔH^\ddagger (kcal/mol) ^a	Mo–O distance at TS (Å)	Mo–O MBO at TS	energy gap (eV) ^b	mix ^c
(1)	$[\text{MoO}_2(\text{mnt})_2]^{2-}$	$\text{P}(\text{OMe})_3$	−48	11(30)	1.83	1.17	4.2	21%
(4)	$[\text{MoO}_2(\text{mnt})_2]^{2-}$	SO_3^{2-}	−39	1(13)	1.78	1.54	1.2	35%
(5)	$[\text{MoO}_2(\text{mnt})(\text{SCH}_3)]^-$	$\text{P}(\text{OMe})_3$	−25	14(25)	1.83	1.17	4.0	23%
(6)	$[\text{MoO}_2(\text{bdt})(\text{SCH}_3)]^-$	$\text{P}(\text{OMe})_3$	−20	16(25)	1.85	1.13	4.0	22%
(7) ^d	$[\text{MoO}_2(\text{bdt})(\text{SCH}_3)]^-$	SO_3^{2-}	−23	3(12)	1.82	1.41	1.4	41%
(8) ^e	$[\text{MoO}_2(\text{bdt})(\text{SCH}_3)]^-$	SO_3^{2-}	−12	32(38)	1.82	1.39	1.1	39%

^aIntrinsic barriers show in parentheses. ^bEnergy gap between the substrate lone pair and the LUMO of the Mo site in reactant. ^cAmount of substrate lone pair mixed into the unoccupied orbitals at the transition state. ^dIn this reaction, the product sulfate stayed bound to the Mo site, which remains a five-coordinate site. ^eThe reaction was carried out with a dielectric constant of 4. There is no stable ES or EP complex, and the resultant four-coordinate Mo^{IV} site rearranged to a trigonal pyramidal geometry.

In reaction (1), the Mo site goes from six-coordinate to five-coordinate, while in reaction (5) one of the dithiolenes is replaced with one thiolate, and the oxo transfer to phosphite corresponds to a five-coordinate to four-coordinate conversion. Reaction (5) has less driving force than (1) due to the difference in Mo–oxo bond strengths (102 kcal/mol for the six-coordinate and 126 kcal/mol for the five-coordinate Mo^{VI} –bisoxo complex); however, the intrinsic barrier for reaction (5) is lower (Table 3). For the six-coordinate $[\text{Mo}^{\text{VI}}\text{O}_2(\text{mnt})_2]^{2-}$, the two oxo atoms are equivalent (9% of each in the LUMO, Figure 10A), and need to polarize toward the oxo that is

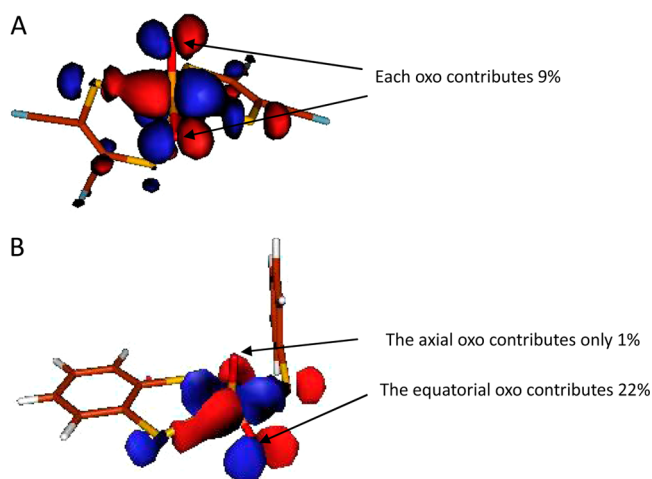


Figure 10. (A) LUMO of six-coordinate $\text{Mo}^{\text{VI}}\text{O}_2$ site. The two oxo atoms are identical in the reactant. (B) LUMO of the five-coordinate Mo^{VI} site. The equatorial oxo atom has a much larger contribution than the axial oxo atom.

transferred (Figure 8B). In the five-coordinate $[\text{Mo}^{\text{VI}}\text{O}_2(\text{mnt})(\text{SCH}_3)]^-$ complex, the two oxo atoms are nonequivalent with the equatorial oxo contributing 22% to the LUMO (1% for the axial oxo, Figure 10B). This activates the equatorial oxo for transfer, consistent with the selectivity of the enzyme.

Another advantage of the five-coordinate Mo^{VI} bisoxo complex is that for a six-coordinate dithiolene complex, the two dithiolene planes have to rotate by about 90° for each reaction cycle. From section 3.3.1, this rotation costs ~ 25 kcal/mol. The energy would be even higher in the enzyme where the pyranopterin extends into the protein. Less dithiolene rearrangement is required in the five-coordinate Mo^{VI} bisoxo site as the major change is simply equatorial oxo transfer.

In going from reaction (5) to (6), the mnt is changed into the bdt, without a change in the intrinsic barrier, and reaction (7) simulates the active site of the native enzyme with the native substrate. Relative to reaction (6) with phosphite, sulfite lowers the reaction barrier and leads to an earlier transition state, as discussed above. The product SO_4^{2-} remains bound to the Mo^{IV} monooxo product complex. The calculated ΔG^\ddagger is 4 kcal/mol, while based on the rate constant ($7.0 \times 10^6 \text{ M}^{-1} \text{ s}^{-1}$ at 298 K),⁵⁴ the experimental ΔG^\ddagger for chicken liver sulfite oxidase is ~ 7 kcal/mol. All the calculations above were done in acetonitrile, which has a dielectric constant of 36. However, in proteins, the dielectric constant is decreased.⁵⁵ Reaction (8) repeated reaction (7) with a dielectric constant of 4. This resulted in a large increase in reaction barrier with no stable ES complex, due to the increase in Coulomb repulsion. The Mo site has a total charge of -1 , while the sulfite has a charge of

-2 . This suggests that in SO, the protein environment contributes to the substrate binding (a positively charged pocket with conserved tyrosine, histidine, and arginine residues) to form the ES complex to lower the barrier for oxo transfer,^{56,57} while the pyranopterin cofactor functions as a pathway to reoxidize the Mo site subsequent to the oxo transfer.^{22,58} [Note that the $\text{O}_{\text{ax}}\text{--Mo--S}_{\text{thiolate}}\text{--C}$ dihedral angle in the optimized structure is different from that in the crystal structure (148° vs 78°). However, this dihedral angle distortion only costs a few kcal/mol of energy, consistent with ref 55.]

In contrast, the experimental ΔG^\ddagger for *Escherichia coli* DMSO reductase is ~ 9 kcal/mol (based on the rate constant $4.3 \times 10^5 \text{ M}^{-1} \text{ s}^{-1}$ at 298 K),⁵⁹ much lower than the value calculated for the model complex (30 kcal/mol).¹⁰ This indicates that the geometry of the enzyme active site is distorted toward the transition state by the protein environment to assist the oxo transfer reaction in DMSO or as suggested by Hall and co-workers¹⁵ and Kirk and co-workers.¹³ Also, in this class of oxo transfer enzymes, the two pyranopterin are found to be structurally different with the protein tuning one to be an electron conduit, to effectively reduce the oxidized state.⁵⁸

5. CONCLUSIONS

This study provides insight into the oxo transfer reaction in sulfite oxidase, based on experimental and computational results on its model complexes, and its relation to our previous studies on related DMSO reductase models. In DMSO, it is the oxo transfer that leads to electron transfer, while in SO, oxo transfer is initiated by the electron transfer. This difference reflects the large energy gap between the LUMO of DMSO and $d\pi$ HOMO in the Mo^{IV} desoxo complex relative to the small energy gap between the sulfite lone pair HOMO and the $d\pi$ orbital-based LUMO of the Mo^{VI} bisoxo complex. The five-coordinate Mo^{VI} bisoxo active site of SO activates the equatorial oxo, and minimizes the reorganization energy over the reaction cycle.

■ ASSOCIATED CONTENT

Supporting Information

Fits to the second derivative of the S K-edge XAS data; electronic structures of $[\text{Mo}^{\text{IV}}(\text{OSi})(\text{bdt})_2]^-$ and $[\text{Mo}^{\text{VI}}\text{O}(\text{OSi})(\text{bdt})_2]^-$ complexes from our previous study; reaction coordinate of reaction (2) without proton shift; reaction coordinate and TS structure compare for oxo transfer from Mo^{VI} complexes to phosphine; fragment energy contribution and TS structure compare for oxo transfer from DMSO to Mo^{IV} complexes; computational results with BP86 functional; computational results comparison of Mo complexes with bdt, mnt, and mdt ligands. Cartesian coordinates for all optimized structures in zipped .xyz files. This material is available free of charge via the Internet at <http://pubs.acs.org>.

■ AUTHOR INFORMATION

Corresponding Authors

holm@chemistry.harvard.edu
hodgson@ssrl.slac.stanford.edu
hedman@ssrl.slac.stanford.edu
solomone@stanford.edu

Present Address

[†]Target Discovery, Inc., Palo Alto, CA 94303

Notes

The authors declare no competing financial interest.

■ ACKNOWLEDGMENTS

This study was supported by NSF grant (CHE 0948211, E.I.S. at Stanford University and CHE 0846397, R.H.H. at Harvard University) and NIH Grant (P41GM103393, K.O.H.). Use of the Stanford Synchrotron Radiation Lightsource, SLAC National Accelerator Laboratory, is supported by the U.S. Department of Energy, Office of Science, Office of Basic Energy Sciences under Contract No. DE-AC02-76SF00515. The SSRL Structural Molecular Biology Program is supported by the DOE Office of Biological and Environmental Research, and by the National Institutes of Health, National Institute of General Medical Sciences (including P41GM103393).

■ REFERENCES

- (1) Hille, R. *Trends Biochem. Sci.* **2002**, *27*, 360.
- (2) Burgess, B. K.; Lowe, D. J. *Chem. Rev.* **1996**, *96*, 2983.
- (3) Howard, J. B.; Rees, D. C. *Chem. Rev.* **1996**, *96*, 2965.
- (4) Holm, R. H.; Kennepohl, P.; Solomon, E. I. *Chem. Rev.* **1996**, *96*, 2239.
- (5) Kisker, C.; Schindelin, H.; Rees, D. C. *Annu. Rev. Biochem.* **1997**, *66*, 233.
- (6) Hille, R. *Chem. Rev.* **1996**, *96*, 2757.
- (7) Schwarz, G.; Mendel, R. R.; Ribbe, M. W. *Nature* **2009**, *460*, 839.
- (8) Tenderholt, A. L.; Szilagyi, R. K.; Holm, R. H.; Hodgson, K. O.; Hedman, B.; Solomon, E. I. *J. Inorg. Biochem.* **2007**, *101*, 1594.
- (9) Enemark, J. H.; Cooney, J. J. A.; Wang, J.-J.; Holm, R. H. *Chem. Rev.* **2004**, *104*, 1175.
- (10) Tenderholt, A. L.; Wang, J.-J.; Szilagyi, R. K.; Holm, R. H.; Hodgson, K. O.; Hedman, B.; Solomon, E. I. *J. Am. Chem. Soc.* **2010**, *132*, 8359.
- (11) George, G. N.; Nelson, K. J.; Harris, H. H.; Doonan, C. J.; Rajagopalan, K. V. *Inorg. Chem.* **2007**, *46*, 3097.
- (12) Pushie, M. J.; Cotelesage, J. J. H.; Lyashenko, G.; Hille, R.; George, G. N. *Inorg. Chem.* **2013**, *52*, 2830.
- (13) McNaughton, R. L.; Lim, B. S.; Knottenbel, S. Z.; Holm, R. H.; Kirk, M. L. *J. Am. Chem. Soc.* **2008**, *130*, 4628.
- (14) Hofmann, M. *Inorg. Chem.* **2008**, *47*, 5546.
- (15) Webster, C. E.; Hall, M. B. *J. Am. Chem. Soc.* **2001**, *123*, 5820.
- (16) Lim, B. S.; Willer, M. W.; Miao, M.; Holm, R. H. *J. Am. Chem. Soc.* **2001**, *123*, 8343.
- (17) Das, S. K.; Chaudhury, P. K.; Biswas, D.; Sarkar, S. *J. Am. Chem. Soc.* **1994**, *116*, 9061.
- (18) Thomson, L. M.; Hall, M. B. *J. Am. Chem. Soc.* **2001**, *123*, 3995.
- (19) Schultz, B. E.; Gheller, S. F.; Muetterties, M. C.; Scott, M. J.; Holm, R. H. *J. Am. Chem. Soc.* **1993**, *115*, 2714.
- (20) Kail, B. W.; Pérez, L. M.; Zarić, S. D.; Millar, A. J.; Young, C. G.; Hall, M. B.; Basu, P. *Chem.—Eur. J.* **2006**, *12*, 7501.
- (21) Mitra, J.; Sarkar, S. *Inorg. Chem.* **2013**, *52*, 3032.
- (22) Peariso, K.; Helton, M. E.; Duesler, E. N.; Shadle, S. E.; Kirk, M. L. *Inorg. Chem.* **2007**, *46*, 1259.
- (23) Tucci, G. C.; Donahue, J. P.; Holm, R. H. *J. Am. Chem. Soc.* **1998**, *37*, 1602.
- (24) Solomon, E. I.; Hedman, B.; Hodgson, K. O.; Dey, A.; Szilagyi, R. K. *Coord. Chem. Rev.* **2005**, *249*, 97.
- (25) Sarangi, R.; George, S. D.; Rudd, D. J.; Szilagyi, R. K.; Ribas, X.; Rovira, C.; Almeida, M.; Hodgson, K. O.; Hedman, B.; Solomon, E. I. *J. Am. Chem. Soc.* **2007**, *129*, 2316.
- (26) Dey, A.; F. E. J., Jr.; Adams, M. W. W.; Babini, E.; Takahashi, Y.; Fukuyama, K.; Hodgson, K. O.; Hedman, B.; Solomon, E. I. *Science* **2007**, *318*, 1464.
- (27) Donahue, J. P.; Goldsmith, C. R.; Nadiminti, U.; Holm, R. H. *J. Am. Chem. Soc.* **1998**, *120*, 12869.
- (28) George, G. N.; EXAFSPAK; Stanford Synchrotron Radiation Laboratory: Menlo Park, CA, 1990.
- (29) Tenderholt, A. L.; Hedman, B.; Hodgson, K. O. *AIP Conf. Proc.* **2006**, *882*, 105.
- (30) Frisch, M. J.; Trucks, G. W.; Schlegel, H. B.; Scuseria, G. E.; Robb, M. A.; Cheeseman, J. R.; Scalmani, G.; Barone, V.; Mennucci, B.; Petersson, G. A.; Nakatsuji, H.; Caricato, M.; Li, X.; Hratchian, H. P.; Izmaylov, A. F.; Bloino, J.; Zheng, G.; Sonnenberg, J. L.; Hada, M.; Ehara, M.; Toyota, K.; Fukuda, R.; Hasegawa, J.; Ishida, M.; Nakajima, T.; Honda, Y.; Kitao, O.; Nakai, H.; Vreven, T.; Montgomery, J. A.; Peralta, J. E.; Ogliaro, F.; Bearpark, M.; Heyd, J. J.; Brothers, E.; Kudin, K. N.; Staroverov, V. N.; Kobayashi, R.; Normand, J.; Raghavachari, K.; Rendell, A.; Burant, J. C.; Iyengar, S. S.; Tomasi, J.; Cossi, M.; Rega, N.; Millam, J. M.; Klene, M.; Knox, J. E.; Cross, J. B.; Bakken, V.; Adamo, C.; Jaramillo, J.; Gomperts, R.; Stratmann, R. E.; Yazyev, O.; Austin, A. J.; Cammi, R.; Pomelli, C.; Ochterski, J. W.; Martin, R. L.; Morokuma, K.; Zakrzewski, V. G.; Voth, G. A.; Salvador, P.; Dannenberg, J. J.; Dapprich, S.; Daniels, A. D.; Farkas, Foresman, J. B.; Ortiz, J. V.; Cioslowski, J.; Fox, D. J. *Gaussian 09*; Gaussian, Inc.: Wallingford, CT, 2009.
- (31) Becke, A. D. *J. Chem. Phys.* **1993**, *98*, 5648.
- (32) Perdew, J. P. *Phys. Rev. B* **1986**, *33*, 8822.
- (33) Lee, C.; Yang, W.; Parr, R. G. *Phys. Rev. B* **1988**, *37*, 785.
- (34) Andrae, D.; Häußermann, U.; Dolg, M.; Stoll, H.; Preuß, H. *Theor. Chim. Acta* **1990**, *77*, 123.
- (35) Hratchian, H. P.; Schlegel, H. B. In *Theory and Application of Computational Chemistry: The First Forty Years*; Dykstra, C. E., Frenking, G., Kim, K. S., Scuseria, G. E., Eds.; Elsevier B. V.: 2005; p 195.
- (36) Tomasi, J.; Mennucci, B.; Cammi, R. *Chem. Rev.* **2005**, *105*, 2999.
- (37) Tenderholt, A. L. In *QMForge*, V2.1; Stanford University: Stanford, CA, 2007.
- (38) O'boyle, N. M.; Tenderholt, A. L.; Langner, K. M. *J. Comput. Chem.* **2008**, *29*, 839.
- (39) Musgrave, K. B.; Donahue, J. P.; Lorber, C.; Holm, R. H.; Hedman, B.; Hodgson, K. O. *J. Am. Chem. Soc.* **1999**, *121*, 10297.
- (40) Tenderholt, A. L.; Szilagyi, R. K.; Holm, R. H.; Hodgson, K. O.; Hedman, B.; Solomon, E. I. *Inorg. Chem.* **2008**, *47*, 6382.
- (41) Szilagyi, R. K.; Lim, B. S.; Glaser, T.; Holm, R. H.; Hedman, B.; Hodgson, K. O.; Solomon, E. I. *J. Am. Chem. Soc.* **2003**, *125*, 9158.
- (42) Lee, S. C.; Holm, R. H. *Inorg. Chim. Acta* **2008**, *361*, 1166.
- (43) Watt, G. D.; McDonald, J. W.; Newton, W. E. *J. Less-Common Met.* **1977**, *54*, 415.
- (44) Holm, R. H.; Donahue, J. P. *Polyhedron* **1993**, *12*, 571.
- (45) Harlan, E. W.; Berg, J. M.; Holm, R. H. *J. Am. Chem. Soc.* **1986**, *108*, 6992.
- (46) Rappe, A. K.; Goddard, W. A. *J. Am. Chem. Soc.* **1982**, *104*, 3287.
- (47) Mayer, I. *Chem. Phys. Lett.* **1983**, *97*, 270.
- (48) Thapper, A.; Deeth, R. J.; Nordlander, E. *Inorg. Chem.* **2002**, *41*, 6695.
- (49) Pauling, L. *J. Am. Chem. Soc.* **1947**, *69*, 542.
- (50) Pal, K.; Chaudhury, P. K.; Sarkar, S. *Chem.—Asian J.* **2007**, *2*, 956.
- (51) Marcus, R. A. *J. Phys. Chem.* **1968**, *72*, 891.
- (52) Chow, M. S.; Liu, L. V.; Solomon, E. I. *Proc. Natl. Acad. Sci. U.S.A.* **2008**, *105*, 13241.
- (53) Tenderholt, A. L.; Hodgson, K. O.; Hedman, B.; Holm, R. H.; Solomon, E. I. *Inorg. Chem.* **2012**, *51*, 3436.
- (54) Brody, M. S.; Hille, R. *Biochemistry* **1999**, *38*, 6668.
- (55) Li, L.; Li, C.; Zhang, Z.; Alexov, E. *J. Chem. Theory Comput.* **2013**, *9*, 2126.
- (56) Rajapaksha, A.; Johnson-Winters, K.; Nordstrom, A. R.; Meyers, K. T.; Emesh, S.; Astashkin, A. V.; Enemark, J. H. *Biochem.* **2010**, *49*, 5154.
- (57) Bailey, S.; Rapson, T.; Johnson-Winters, K.; Astashkin, A. V.; Enemark, J. H.; Kappler, U. *J. Biol. Chem.* **2009**, *284*, 2053.
- (58) Rothery, R. A.; Stein, B.; Solomonson, M.; Kirk, M. L.; Weiner, J. H. *Proc. Natl. Acad. Sci. U.S.A.* **2012**, *109*, 14773.
- (59) Cobb, N.; Hemann, C.; Polsinelli, G. A.; Ridge, J. P.; McEwan, A. G.; Hille, R. *J. Biol. Chem.* **2007**, *282*, 35519.